Angewandte Chemie International Edition

Angewandte International Edition Chemie

GDCh German Chemical Society

How to cite: *Angew. Chem. Int. Ed.* **2026**, 65, e25311
doi.org/10.1002/anie.202525311

RESEARCH ARTICLE OPEN ACCESS Hot Paper

Trinuclear Heptamethine Dyes for Shortwave Infrared In Vivo Imaging

Cesar A. Garcia[1] | Eric Y. Lin[1] | Emily B. Mobley[1] | Allen Louie[2,3] | Kaitlin M. Hartung[1] | Jesus A. Araujo[2,3,4,5] | Ellen M. Sletten[1,6,7]

[1]Department of Chemistry and Biochemistry, University of California, Los Angeles, California, USA | [2]Division of Cardiology, David Geffen School of Medicine, University of California, Los Angeles, California, USA | [3]Environmental and Molecular Toxicology Interdepartmental Program, University of California, Los Angeles, California, USA | [4]Department of Environmental Health Sciences, Fielding School of Public Health, University of California, Los Angeles, California, USA | [5]Molecular Biology Institute, University of California, Los Angeles, California, USA | [6]California NanoSystems Institute, University of California, Los Angeles, California, USA | [7]Jonsson Comprehensive Cancer Center, University of California, Los Angeles, California, USA

Correspondence: Ellen M. Sletten (sletten@chem.ucla.edu)

Received: 16 November 2025 | **Revised:** 4 February 2026 | **Accepted:** 5 February 2026

Keywords: fluorescent probes | imaging agents | near infrared | polymethine dyes | shortwave infrared

ABSTRACT

The term polymethine dye (PMD) has been intimately connected to the dinuclear scaffold–two heterocycles linked together by a polymethine chain of varying length. Dinuclear PMDs have been a successful scaffold for noninvasive in vivo imaging in the biologically advantageous near infrared (NIR) and shortwave infrared (SWIR) regions of the electromagnetic spectrum. Trinuclear PMDs, resulting from the addition of a third heterocycle into the polymethine chain, possess the same photophysical properties that make dinuclear dyes excellent fluorescent probes, but have yet to be investigated for in vivo imaging. Herein, we expand upon the dinuclear and trinuclear heptamethine dye scaffolds by taking advantage of the increased reactivity of a cyclopentenyl linker and synthesizing flavylium- and chromenylium-based SWIR-emitting fluorophores. The trinuclear scaffold instills the fluorophores with increased steric bulk, leading to beneficial photophysical properties in micelles and outperforming their classic dinuclear counterparts. In this work, we apply trinuclear PMDs for in vivo SWIR imaging in mice and find them to be particularly efficient at lymph node labeling upon intravenous administration.

1 | Introduction

Polymethine dyes (PMDs) have exploded in popularity due to their intense absorptive properties and fluorescent nature [1, 2]. The polymethine chain gives PMDs their defining feature: the delocalization of π-electrons across a conjugated methine chain linking electron-rich heterocycles [3, 4]. PMDs have a small ground-to-first excited state absorption band, resulting in narrow absorption and emission profiles –ideal photophysical properties for optical imaging [3]. These scaffolds have been successful as contrast agents for optical imaging applications in the visible (Vis, 400–700 nm), near infrared (NIR, 700–1000 nm), and shortwave infrared (SWIR, 1000–2000 nm) regions of the electromagnetic spectrum [5–10]. The NIR and SWIR are optimal regions to perform in vivo imaging due to the enhanced penetration of low-energy light through tissue, and decreased background autofluorescence of endogenous emitters [11].

A selection of PMDs have been reported to preferentially accumulate in specific organs, cell types, or tissues. This localization is dependent on the chemical structure of the dye [12–14]. Traditional PMDs have shown notable accumulation in solid tumors (e.g., prostate and gastric cancer), bone, cartilage, and lymph nodes. The versatility in tissue specificity has been

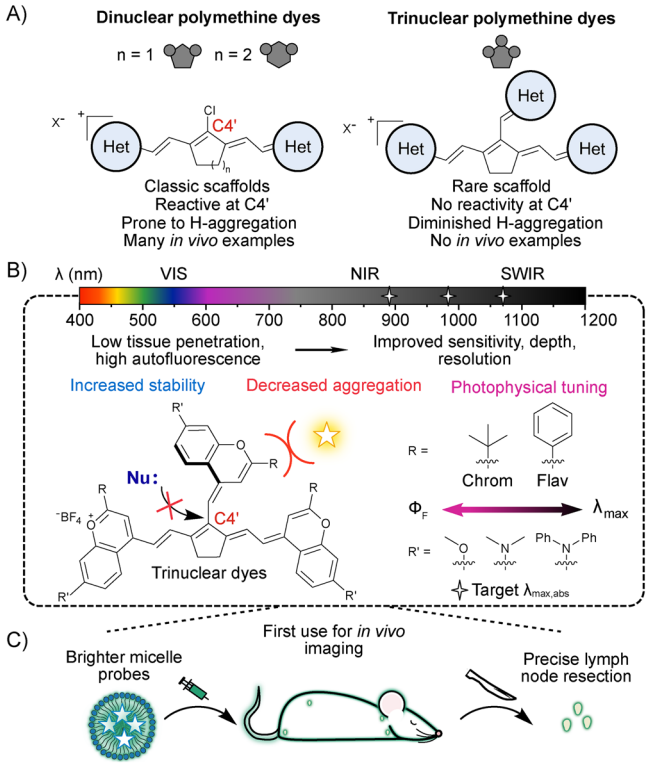

FIGURE 1 | Polymethine dye structures and advantages. (A) Cyclohexenyl- and cyclopentenyl-bearing dinuclear and trinuclear heptamethine dyes. (B) Trinuclear heptamethine dyes are reported herein with schematized advantages of increased stability and decreased aggregation due to the heterocycle appended at the C4' position. (C) This work: First use of trinuclear heptamethine dyes for in vivo imaging.

leveraged for applications in optical imaging, photodynamic therapy, photothermal therapy, and tumor resection [12, 13, 15–20]. Consequently, modifications to PMDs not only modulate the photophysical properties and stability of the fluorophore, but also enable new biological applications.

The overwhelming majority of PMDs are composed of two heterocycles, the so-called dinuclear scaffolds. Trinuclear scaffolds, defined by the addition of a third heterocycle into the polymethine chain, have also been reported (Figure 1A) [5, 21–25], but insight into the biodistribution patterns of trinuclear PMDs is currently sparse. One of the most studied examples in the literature is NK-4, a quinolinium-based trinuclear pentamethine dye which has been explored for its anti-oxidative, anti-cancer, and neuroprotective effects [26–28]. Overall, there is significant room for expanding the fundamental understanding and utility of trinuclear PMDs for in vivo imaging.

While trinuclear heptamethine dyes were first reported almost 50 years ago, they remain an underexplored scaffold for optical imaging. Herein, we use previously established heterocycles for SWIR fluorophores to synthesize bright chlorocyclopentenyl-bearing dinuclear heptamethine dyes. Taking advantage of the increased susceptibility for nucleophilic addition at the central position (C4') of these dinuclear fluorophores, we synthesize trinuclear heptamethine dyes, expanding upon the current synthetic toolbox toward chromenylium PMDs (Figure 1B). In comparison to their dinuclear counterparts, the trinuclear dyes demonstrate improved chemical stability and advantageous photophysical properties in micelles, a delivery vehicle commonly used for in vivo imaging. These findings prompted exploration for their first use as contrast agents for in vivo SWIR imaging, enabling the labeling and subsequent image-guided resection of lymph nodes (Figure 1C).

2 | Results and Discussion

2.1 | Trinuclear Flavylium- and Chromenylium-Based Heptamethine Dyes

Previously, we have synthesized a diverse panel of flavylium- and chromenylium-based cyclohexenyl-bridged heptamethine SWIR-emissive fluorophores and applied them to in vivo imaging [29–32]. Chromenylium and flavylium heterocycles balance high absorption coefficients, SWIR emission, and favorable biological compatibility when incorporated into PMD scaffolds. These heterocycles have consistently provided some of the brightest small-molecule SWIR emitters [29–32]. Furthermore, their modular synthetic accessibility enables facile electronic tuning of absorption maxima, facilitating precise matching of $\lambda_{max,abs}$ to common NIR and SWIR laser lines, which maximizes signal and enables multiplexed imaging [30–32]. These fluorophores can also be elaborated with versatile functional groups to tailor them to a variety of applications. Recent developments include incorporation into star polymer architectures to imbue protein-repelling "stealth" behavior in vivo, as well as addition of charged moieties to enable aqueous solubility, cell tracking, and bone imaging [20, 33].

In an effort to expand chromenylium and flavylium heptamethine dinuclear PMDs further into the SWIR region, we exchanged the cyclohexenyl-bridged linker with a cyclopentenyl ring, expecting a moderate red-shift [35–37]. We began our exploration of cyclopentenyl-bridged PMDs with a dimethylamino-substituted flavylium heterocycle (**1**). Heterocycle **1** yields **Flav7** when condensed with a cyclohexenyl linker, *N*-((*E*)-((*E*)-2-chloro-3-((phenylamino)methylene)cyclohex-1-en-1-yl)methylene)benzenaminium chloride, at 100°C in a *n*-BuOH:PhMe mixture. Repeating these conditions with the cyclopentenyl linker, (*E*))-((*E*)-2-chloro-3-((phenylamino)methylene)cyclopent-1-en-1-yl)methylene)benzenaminium chloride, produced a cyclopentenyl-bridged flavylium-based fluorophore (**2**) in 39% yield. Notably, with long reaction times, we also observed the addition of a third heterocycle to form a trinuclear heptamethine, **3** (Figure 2A). Optimization of the reaction with 3 equivalents of heterocycle **1** and switching the solvent to Ac_2O favored the formation of **3,** and resulted in a 42% yield. We postulated that the reaction mechanism undergoes an S_NAr pathway due to the increased stabilization of the negative charge within a Meisenheimer complex in solvents of higher polarity, increasing reactivity at the C4' position [38, 39].

Having prepared the new dinuclear polymethine **2** and trinuclear polymethine **3**, we investigated their photophysical properties compared to **Flav7** (Figure 2B). As expected, the $\lambda_{max,abs}$ of the cyclopentenyl-containing dinuclear PMD **2** was bathochromically shifted 30 nm from that of **Flav7**. Interestingly, the

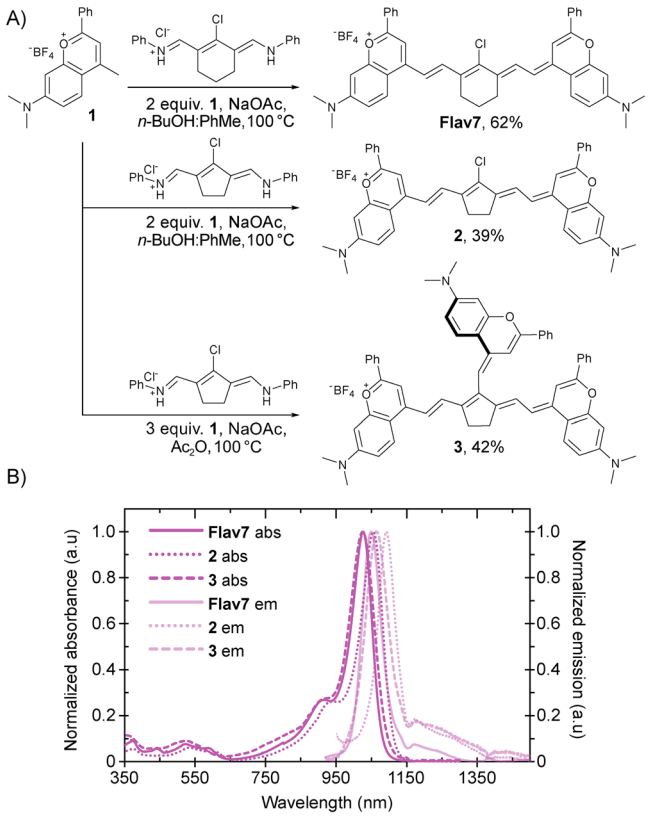

FIGURE 2 | Synthesis and characterization of flavylium dinuclear and trinuclear polymethine dyes. (A) Reaction schemes to access **Flav7**, **2**, and **3**. (B) Normalized absorbance and emission spectra of di- and trinuclear polymethine dyes in dichloromethane. Absorbance (abs) samples were 2.1–2.7 μM and emission (em) samples were 0.4–0.7 μM. Ex. = 885 nm.

absorption profile of the trinuclear PMD, **3**, matched that of **Flav7**, providing an alternative fluorophore scaffold at that $\lambda_{max,abs}$. The absorption coefficients (ε_{max}) of **2** and **3** were similar to those of **Flav7**. The emission properties of all three fluorophores were also similar, with a small increase in Stokes shift (38, 33 nm for **2**, **3** vs. 26 nm for **Flav7**) and a small decrease in quantum yield of fluorescence (Φ_F, 0.54%, 0.53% for **2**, **3** vs. 0.61% for **Flav7**) observed for **2** and **3** when compared to **Flav7**. Overall, the photophysical properties of the trinuclear PMDs appear promising for their use as SWIR contrast agents.

2.2 | Panel of Trinuclear Polymethine Dyes

In addition to the tissue penetration and enhanced signal-to-noise ratios that can be achieved using SWIR light, a major advantage of imaging in the SWIR region is its wider range of wavelengths that can be used for imaging through tissue. An important consideration in the design of SWIR-emitting fluorophores is how to maximize the amount of signal beyond 1000 nm. Due to the energy gap law, NIR and SWIR fluorophores suffer from low quantum yields of fluorescence, which significantly impact brightness (brightness = $\Phi_F \times \varepsilon_{max}$) [3]. Therefore, the design of SWIR contrast agents benefits from careful matching of the $\lambda_{max,abs}$ with the excitation wavelength to maximize the number of photons absorbed, thereby overcoming these intrinsic limitations in emission. We have previously showcased this through the preparation of fluorophores spanning the NIR and SWIR that are well-matched to common laser lines [30–32]. The finding that the trinuclear PMDs have very similar $\lambda_{max,abs}$ as the chlorocyclohexenyl-containing dinuclear PMDs guided the design of trinuclear PMDs for in vivo imaging at three standard laser lines: 890, 974, and 1060 nm.

To match these laser lines, we chose dimethylamino-substituted chromenylium (**S1**), methoxy-substituted chromenylium (**S2**), and diphenylamino-substituted flavylium (**S3**) as heterocycles (Scheme S1). Reacting three equivalences of each heterocycle readily produced the trinuclear cyclopentenyl-bridged heptamethines **5**, **7**, and **8** in moderate yields, 21–42% (Figure 3A, Scheme S1, see Chart S1 for full structures). The dinuclear cyclopentenyl counterparts **4** and **6** were also synthesized in 28–38% isolated yields (Scheme S2). Unfortunately, the cyclopentenyl-bridged dinuclear heptamethine dye with diphenylamino substituents (derived from heterocycle **S3**) was unstable to isolation conditions. We also briefly explored the synthesis of trinuclear cyclohexenyl-bridged PMDs (**S4**), which produced a crude absorption spectrum with $\lambda_{max,abs}$ = 944 nm (Figure S1), but faced difficulties in isolating the fluorophore due to degradation during purification procedures.

Having synthesized a set of SWIR-emitting dinuclear and trinuclear cyclopentenyl-bridged PMDs, we investigated their photophysical properties and compared them to their dinuclear cyclohexenyl-bridged counterparts (Figure 3B). We confirmed that the absorption and emission profiles of trinuclear scaffolds closely match those of their dinuclear cyclohexenyl-bridged counterparts (Figure 3C), verifying our approach to synthesize trinuclear PMDs with $\lambda_{max,abs}$ matching common laser lines. Fluorophore **7** ($\lambda_{max,abs}$ = 925 nm) was designed toward the 890 nm laser, **5** ($\lambda_{max,abs}$ = 975 nm) matches the 974 nm laser, and **8** ($\lambda_{max,abs}$ = 1047 nm) absorbs near the 1060 nm laser. Similar to other reports of trimethine and pentamethine trinuclear PMDs [40–43], we noticed that all trinuclear heptamethine dyes are blue-shifted from their dinuclear cyclopentenyl-bridged counterparts by approximately 25 nm. This blue-shift can be attributed to the lowering of the highest occupied molecule orbital (HOMO) levels in trinuclear PMDs [40]. Moreover, these spectroscopic trends and previous DFT calculations with similar trinuclear scaffolds [44] suggest that the third heterocycle is out-of-plane relative to the polymethine chain, and minimally participates in conjugation across the delocalized π -system. In terms of Φ_F, the cyclopentenyl-containing PMDs are slightly less efficient than their cyclohexenyl-containing counterparts. Fortunately, the high absorption coefficients (ε_{max}, on the order of 10^5 $M^{-1}cm^{-1}$) characteristic of PMDs are maintained.

2.3 | Nucleophilic Stability of Dinuclear and Trinuclear Heptamethine Dyes

With a method to synthesize the trinuclear polymethine scaffold established, we next looked to investigate their nucleophilic stability. Due to the additional heterocycle at the C4' position, we postulated that the fluorophores would display superior stability due to steric hindrance. As such, we compared the stability of

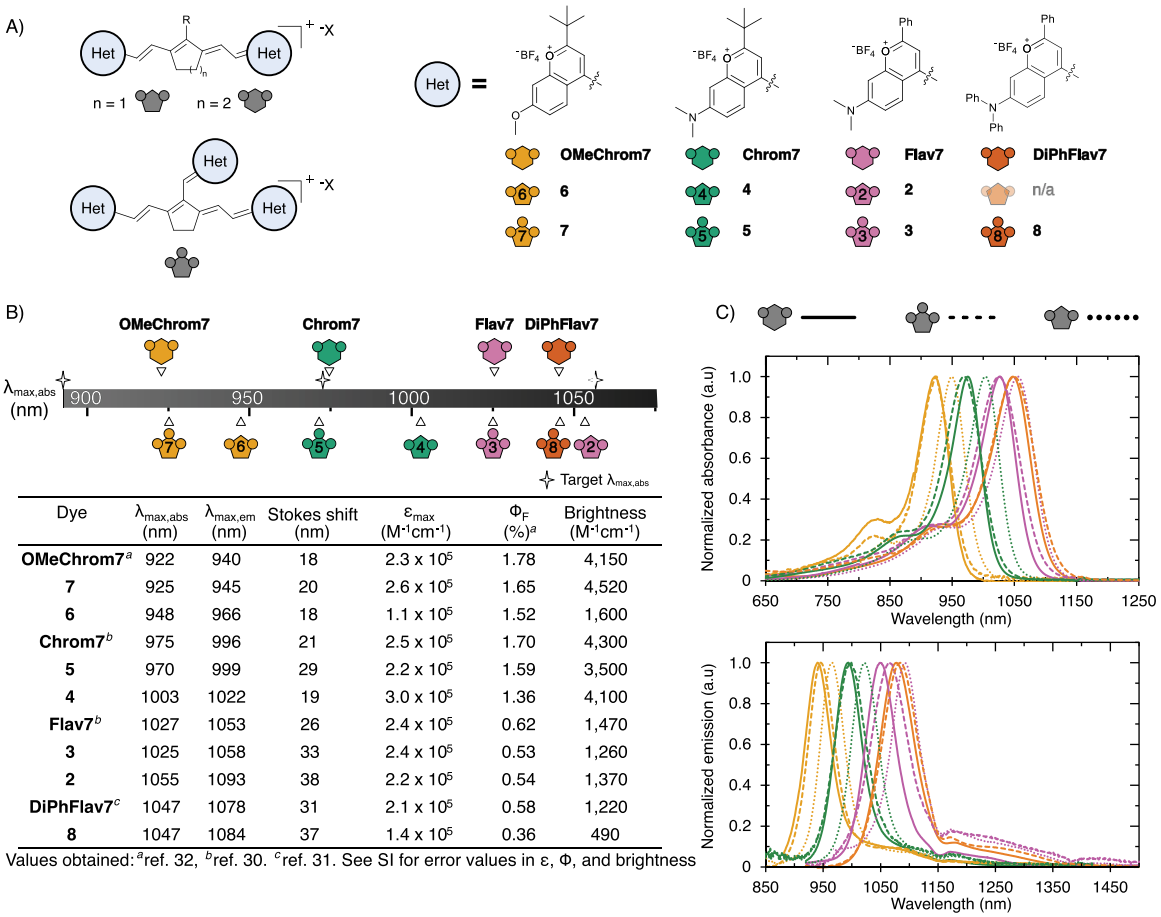

Dye	$\lambda_{max,abs}$ (nm)	$\lambda_{max,em}$ (nm)	Stokes shift (nm)	ε_{max} ($M^{-1}cm^{-1}$)	Φ_F (%)[a]	Brightness ($M^{-1}cm^{-1}$)
OMeChrom7[a]	922	940	18	2.3×10^5	1.78	4,150
7	925	945	20	2.6×10^5	1.65	4,520
6	948	966	18	1.1×10^5	1.52	1,600
Chrom7[b]	975	996	21	2.5×10^5	1.70	4,300
5	970	999	29	2.2×10^5	1.59	3,500
4	1003	1022	19	3.0×10^5	1.36	4,100
Flav7[b]	1027	1053	26	2.4×10^5	0.62	1,470
3	1025	1058	33	2.4×10^5	0.53	1,260
2	1055	1093	38	2.2×10^5	0.54	1,370
DiPhFlav7[c]	1047	1078	31	2.1×10^5	0.58	1,220
8	1047	1084	37	1.4×10^5	0.36	490

Values obtained: [a]ref. 32, [b]ref. 30. [c]ref. 31. See SI for error values in ε, Φ, and brightness

FIGURE 3 | Comparison of photophysical properties of di- and trinuclear polymethine dyes. (A) Panel of published (hexagons) and synthesized (pentagons) heptamethine dyes. (B) Electromagnetic spectrum indicating the absorbance maxima, and a table of photophysical parameters in dichloromethane. See Table S1 for error values associated with measurements. (C) Absorbance and emission spectra in dichloromethane. Absorbance samples were 2.0–5.8 μM, and emission samples were 0.4–2.4 μM. Ex. = 885 nm: **2–5**, **8**; 840 nm: **6–7**. [Correction added on February 23, 2026, after first online publication: Figure 3, Figure 4 and Figure 5 has been updated.]

Chrom7 with its dinuclear and trinuclear cyclopentenyl-bridged analogues **4** and **5**, respectively. We explored the reactivity of this scaffold to nucleophiles bearing thiol, alcohol, and amine functionalities, representative of common endogenous biological nucleophiles. Due to the insolubility of the trinuclear scaffold in water, we pivoted to the use of organic mixtures, which also promote S_NAr reactivity and facilitate the comparison of different PMD scaffolds. When subjecting **Chrom7**, **4**, and **5** to 1.1 equivalences of cysteamine at 50°C in a basic solution of *n*-BuOH:Tol, the increased reactivity of the cyclopentenyl scaffold was apparent. Fluorophore **4** was quantitatively converted to the thiol adduct (**S6**) within 1 h (Figure S2). In contrast, **Chrom7** displayed significantly increased stability with 88% conversion to the thiol adduct over 24 h (Figure S2). Gratifyingly, **5** showed no susceptibility to nucleophilic addition by the thiol substrate, which we attribute to the absence of the chlorine atom at the C4' position and the steric bulk of the third heterocycle. Addition of the weaker nucleophiles, phenol, and butylamine, did not result in as rapid or full conversion to the corresponding products. We observed some reactivity with **4** (phenol = 5%, butylamine = 11%), but none was observed with **Chrom7** or the trinuclear counterpart **5** (Figure S3–S5). Aniline and Boc-L-serine methyl ester displayed no reactivity with any of the fluorophores tested. These data indicate that if the stability of **Chrom7**, **Flav7**, and their similar congeners is a limitation, trinuclear dyes may be a valuable alternative.

2.4 | Micelle Characterization

We next explored the potential for the trinuclear heptamethine dyes, **3**, **5**, **7**, and **8**, to be used as optical imaging agents for in vivo applications. Due to their insolubility in biological media, hydrophobic dinuclear PMDs necessitate a water-solubilizing delivery vehicle, with the most common approach being encapsulation within DSPE-PEG micelles [29–32]. Unfortunately, the extended structural conjugation of SWIR-emissive PMDs is prone to π-stacking, forming nonemissive H-aggregates in the delivery vehicle. This phenomenon results in a blue-shifted, broad absorbance, lowering the concentration of emissive species and diminishing the brightness of the probes [45]. Previously, we have found that substitution at the C4' position can minimize the H-aggregation observed in micelles [32]. Thus, the trinuclear dyes with bulky C4' substituents are poised to have excellent fluorescent properties in micelle formulations.

To understand how the structural differences of the dinuclear and trinuclear scaffolds modulate their aggregation in micelles,

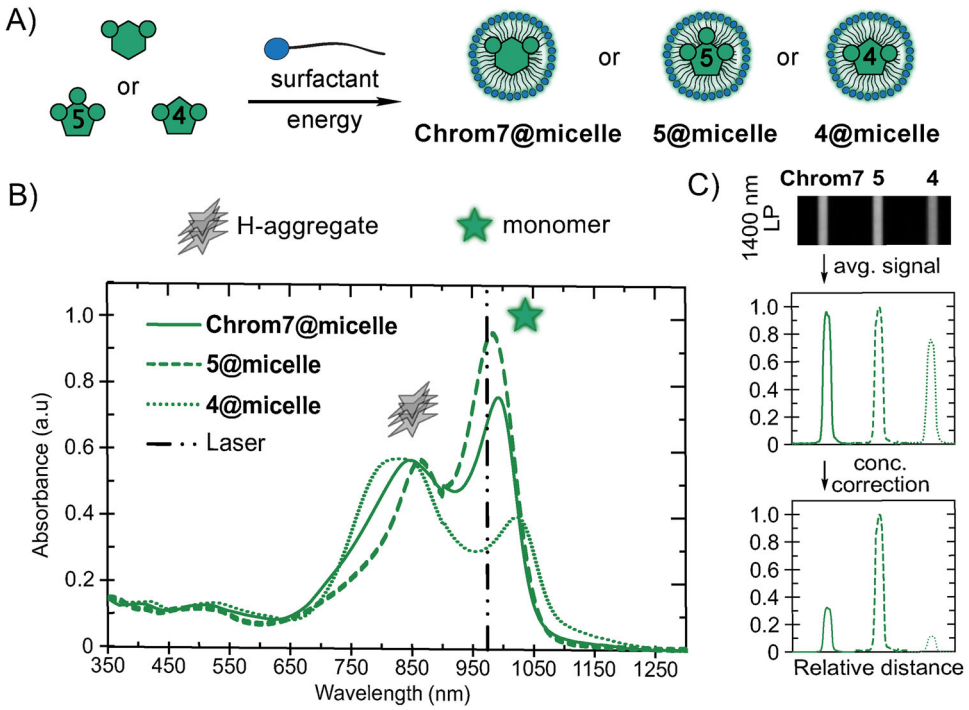

FIGURE 4 | Improved solubility of micelle-encapsulated fluorophores leads to brighter probes. (A) Micelle formulation scheme. (B) Normalized absorbance (with respect to the H-aggregate signal) of **Chrom7@micelles**, **4@micelles**, and **5@micelles** in PBS. (C) Capillary image of absorption-matched micelles in PBS and normalized brightness comparisons with respect to **5@micelles**. Images were captured via InGaAs camera (Ex. = 890 nm, 148 mW cm^{-2}, 1400 nm LP, ET = 100 ms).

we prepared micelles encapsulating **Chrom7**, **4,** or **5** (our best 974 nm laser-matched fluorophores) to form **Chrom7@micelles**, **4@micelles**, and **5@micelles** (Figure 4A and Scheme S3). All micelles were approximately 10 nm in size (Figure S6) and displayed a negative zeta potential, as is typical of DSPE-PEG micelles (**5@micelles** zeta = −6.1 mV, Figure S7). UV-Vis analysis of the micelles revealed significant H-aggregation with **4@micelles**, as observed by the broad absorption at ~820 nm, with a monomer-to-H-aggregate ratio of 0.6:1. In contrast, the trinuclear **5@micelles** showed increased monomeric character (monomer-to-H-aggregate ratio of 2.1:1, Figure 4B) and characteristic SWIR emission (Figure S7), indicating that the increased steric bulk diminishes H-aggregation. Encouraged by these results, we performed a brightness comparison experiment between **4@micelles**, **5@micelles**, and **Chrom7@micelles**, exciting with a 974 nm laser and measuring SWIR emission with an InGaAs camera (Figures 4C and S8). When normalizing for concentration of dye within the micelle, the increased portion of monomer species in the micelle improved the brightness of **5@micelles**, boasting a 3× increase compared to the **Chrom7@micelles**, and a 7× increase compared to the **4@micelles** when using a 1400 nm longpass (LP) filter (Figures 4C and S8). The photobleaching rates of all micelles were measured by illuminating with the 890 nm laser (110 mW cm^{-2}) and detecting the percentage loss in fluorescence. While **Chrom7@micelles** had the lowest relative photobleaching rate (1.09×10^{-25} s^{-1}), trinuclear dye micelles demonstrated increased photobleaching rates relative to **Chrom7@micelles** (**5@micelles**, **7@micelles**, and **8@micelles**: 3.5, 2.1, 2.7, respectively; Figure S9 and Table S2). We investigated if these differences were due to changes in singlet oxygen ($^1O_2$) generation by using the $^1O_2$ trap 9,10-anthracenediyl-bis(methylene)dimalonic acid (ABDA, Figure S10A). However, there was no detectable reactivity of $^1O_2$ with ABDA upon photobleaching **Chrom7@micelles** or **5@micelles** (Figure S10B–D), suggesting other reactive oxygen species are dominant or that $^1O_2$ reacts more rapidly with **5** than ABDA.

2.5 | In Vivo Imaging With Trinuclear Heptamethine Dyes

Ultimately, our goal was to implement the trinuclear polymethine dye scaffold for single-channel SWIR imaging of live mice. We first assessed cell viability of the excitation-matched fluorophores—**5@micelles**, **7@micelles**, **8@micelles**—as well as empty micelles by incubating with A375 cells overnight. Given acceptable cell viability across all PMDs when compared to empty micelles (Figure S11), we began in vivo studies by injecting the brightest probe, **5@micelles**, into anesthetized mice and monitoring the signal over time (Figure 5A). The trinuclear scaffold provided impressive visualization of the vasculature system in great detail with a 1400 nm LP filter as observed from the lateral views of the animal (Figure 5B–E). Immediately after injection, we also observed accumulation in the liver, a common result with micelle-delivered PMDs [29–32, 34]. Interestingly, while we saw signal in the liver over extended periods of time, **5@micelles** also circulated the vasculature over 3 h (Figures 5C and SA1–4), much longer than previously observed with **Chrom7@micelles**, its dinuclear fluorophore analogue. Vasculature imaging, which is critical for blood flow and perfusion studies, is one application

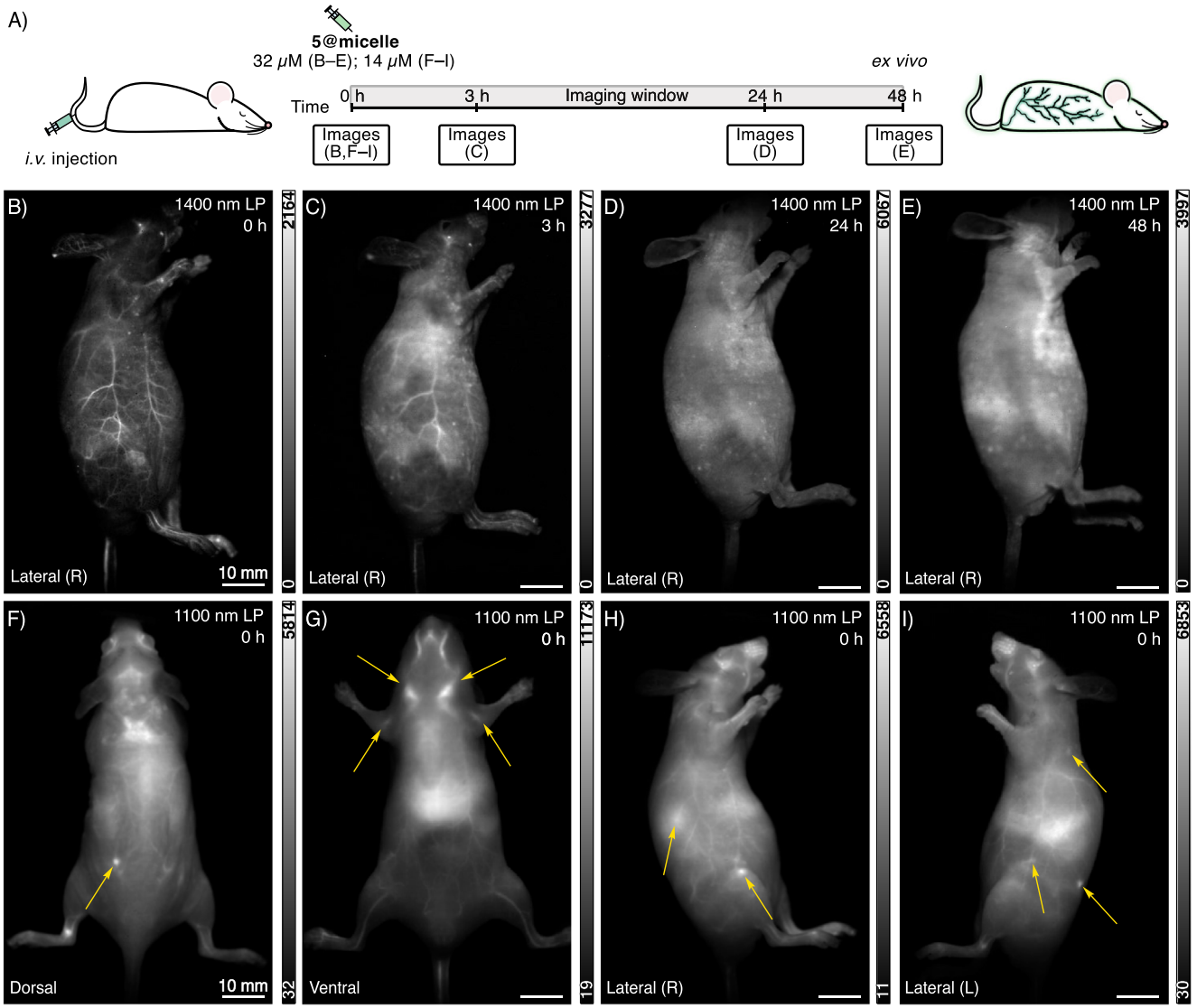

FIGURE 5 | In vivo SWIR imaging of nude mouse i.v. injected with **5@micelles**. (A) Experimental scheme and imaging timeline (not to scale). SWIR images captured via InGaAs camera after i.v. injection of **5@micelle** (32 μM (B–E); 14 μM (F–I), 200 μL injection, Ex. = 974 nm, 152 mW cm^{-2}, 100 ms ET). (B–E): Right lateral view of mouse after injection at t = 0 h (B), 3 h (C), 24 h (D), and 48 h (E). Collect: 1400 nm LP. (F–I): Dorsal (F), ventral (G), right lateral (H), and left lateral (I) views of the mouse at $t = 0$ h. Collect 1100 nm LP (B–E). Scale bars = 10 mm.

where the trinuclear scaffold appears superior to traditional dinuclear PMDs [46].

At 3 h, we also started to observe some accumulation on the skin, which became dominant by 24 h (Figure 5D). At 48 h, the mouse was euthanized, and an ex vivo analysis of internal organs was performed (Figure S12A). This exploration confirmed the typically observed accumulation in the liver, but also revealed a surprising degree of lymph node labeling. Murine lymph nodes are small and are very difficult to resect without a contrast agent [33, 47]. Notably, in mice injected with **5@micelles**, the accumulation within lymph nodes was bright enough to allow for the precise, image-guided necroscopic resection of various lymph nodes (Figure S12B). On a subsequent injection of **5@micelles** at a lower dose, we noticed we were immediately able to noninvasively visualize several lymph nodes (Figures 5F–I, and SA5). Noninvasive detection gradually became more difficult over time, as skin accumulation began to obscure the lymph node signal (Figure SA6–8). However, the lymph nodes remained labeled, enabling image-guided resection (Figure 6A–C, Video S1, SA9).

Next, we investigated the in vivo biodistribution of trinuclear dyes **7** and **8**, which could be imaged upon 890 and 1060 nm excitation, respectively. Again, we encapsulated the fluorophores in micelles, administered them to mice, and imaged over 48 h. For both **7@micelles** and **8@micelles**, lymph node accumulation could also be observed noninvasively at early timepoints (Figure SA10–25). Upon ex vivo analysis, broad lymph node labeling was evident, and image-guided resection resulted in multiple lymph nodes being resected from each mouse (Figure 6D,E, Video S2, and Figure SA26–29). While we have previously observed lymph node labeling with dinuclear PMDs encapsulated in micelles or the FDA-approved PMD indocyanine green (ICG), the rapid and extensive lymph node labeling with the trinuclear PMDs upon intravenous injection was striking.

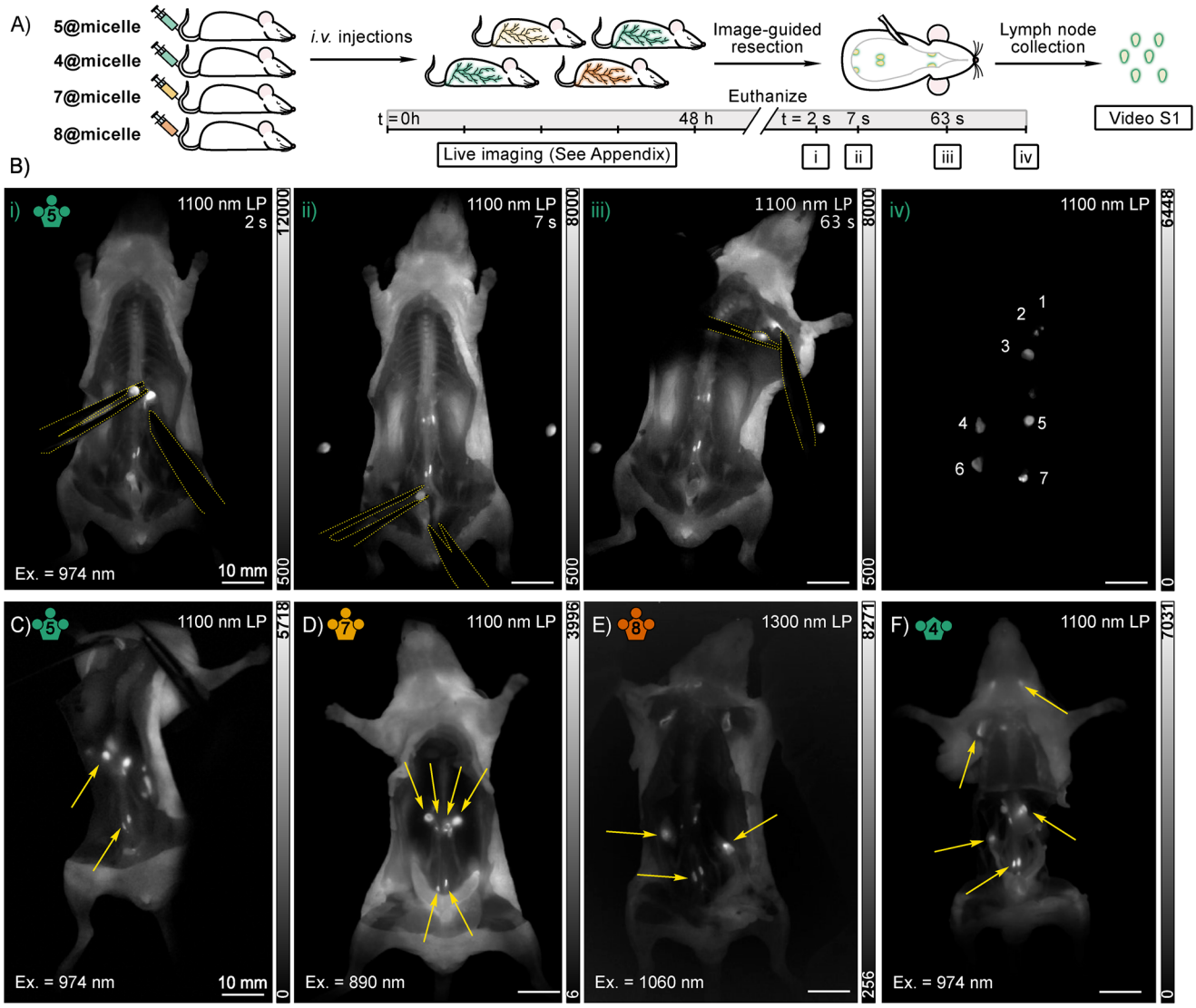

FIGURE 6 | In vivo SWIR images of a nude mouse injected with **dye@micelles** and ex vivo lymph node resection. (A) Scheme of experiment and timeline of SWIR images after i.v. injection of **dye@micelles**. (B) Still images of lymph node resection (i–iii, Video S1) and resected lymph nodes (iv) after injection of **5@micelles** (32 μM, 200 μL, ex. 974 nm, 152 mW cm^{-2}, 2 ms ET. Collect: 1100 nm LP filter). (C) Still images of mouse carcass after injection of **5@micelles**, (D) **7@micelles** (1.4 mM, 200 μL, Ex. 890 nm, 148 mW cm^{-2}, 1 ms ET. Collect: 1100 nm LP filter), (E) **8@micelles** (50 μM, 200 μL, Ex. 1060 nm, 160 mW cm^{-2}, 20 ms ET. Collect: 1300 nm LP filter), and (F) **4@micelles** (250 μM, 200 μL, Ex. 974 nm, 152 mW cm^{-2}, 1 ms ET. Collect: 1100 nm LP filter). Scale bars = 10 mm. Yellow arrows indicate visible lymph nodes. Dashed yellow lines outline the tweezers and scissors used for resection.

Intrigued by the observed systemic lymph node accumulation, we explored a few different hypotheses to explain the observed localization. Previous work has indicated that covalent modification of albumin can lead to preferential lymph node labeling [48, 49], and we searched for evidence of the trinuclear PMDs covalently modifying proteins in vivo. However, despite multiple rounds of ex vivo analysis, we were unable to detect any indication of covalent protein modification, suggesting the labeling is a function of the micelle formulation or noncovalent association of the fluorophore with other biomolecules [50]. To test if the lymph node accumulation was exclusive to the trinuclear scaffold, we formulated the dinuclear cyclopentenyl derivative **4** to yield **4@micelles** and analyzed the biodistribution upon i.v. injection (Figures 6F and SA30–34). We found that **4@micelles** also displayed lymph node labeling; however, we do not recommend the use of **4@micelles**, as a hives-like skin rash was observed one day post-injection. We attribute this adverse reaction to reactivity at the C4' position in vivo, but do not believe this reactivity is related to the lymph node labeling. However, an inflammatory response could be another reason for lymph node accumulation of the micelles [51]. The immune response was probed by culturing **5@micelles**, **7@micelles**, **8@micelles**, and empty micelles, and monitoring the fold-change of inflammatory gene expression (IL-1α, IL-1β, IL-6, TNF-α) in RAW cells, a murine macrophage cell line. These data indicate that the trinuclear micelles do not cause a greater fold change in any inflammatory gene in comparison to empty micelles (Figure S13), which does not support the hypothesis that an immune response is the cause of the observed biodistribution. To test whether the micelle composition may play a role, we formulated **5** with DSPE-mPEG5000 micelles

to yield **5@micelles***, and analyzed the biodistribution upon i.v. injection (Figure SA35–43). **5@micelles*** behaved similarly to **5@micelles**. Upon quantification of organ to lymph node ratios from all mice injected with trinuclear dyes formulated in DSPE-mPEG2000 micelles versus DSPE-mPEG5000 micelles, we observed no statistically significant differences between the two surfactants (Figures S14 and SA44). This analysis also highlights the large biological variability with respect to the degree of lymph node labeling. Ultimately, the root cause of the inherent lymph node accumulation by these fluorophore remains elusive; however, we can conclude that micelles containing trinuclear PMDs are bright, biocompatible, and nonimmunogenic, and have potential for the global imaging of lymph nodes in vivo.

3 | Conclusion

Optical imaging in the NIR and SWIR regions has enhanced how we study biological systems. While the classic PMD scaffold for in vivo imaging has been primarily associated with dinuclear heptamethine dyes, the much rarer trinuclear heptamethine scaffold has never been explored as a contrast agent for this application. Here, we leverage the heightened reactivity of cyclopentenyl-bridged dinuclear heptamethine dyes, introducing a third heterocycle at the C4' position through S_NAr chemistry. We expanded upon this scaffold to synthesize a panel of laser-matched, SWIR-emissive, chromenylium-based cyclopentenyl-bridged trinuclear heptamethine dyes. Compared to their dinuclear analogues, this scaffold exhibited reduced electrophilic reactivity to various biologically relevant nucleophiles. Photophysical studies demonstrated that the high brightness characteristic of previous dinuclear cyclohexenyl heptamethine dyes was retained by the trinuclear scaffold. Moreover, the nearly identical absorption profile and $\lambda_{max,abs}$ to their dinuclear cyclohexenyl counterparts enabled seamless use with existing laser lines for which their cyclohexenyl dinuclear counterparts were designed, circumventing further tedious synthetic modifications to fine-tune absorption maxima. When encapsulated in micelles, the trinuclear scaffold advantage shone, where the steric bulk imparted by the third heterocycle diminished nonemissive H-aggregation, a problem plaguing other hydrophobic PMDs.

This work establishes the utility of trinuclear PMDs for in vivo imaging, expanding beyond the classic dinuclear scaffold. When administered in vivo, these dyes accumulated in lymph nodes, providing high contrast SWIR imaging and enabling the precise, image-guided resection of lymph nodes post-mortem. By combining chemical stability, exceptional SWIR brightness, and lymphatic targeting, these PMDs offer avenues for noninvasive mapping of lymph nodes, surgical guidance, and broader biological imaging applications where deep-tissue penetration and low background are paramount. This study demonstrates that trinuclear heptamethine dyes are a viable alternative scaffold for optical imaging, advancing our capabilities to study biological systems.

Author Contributions

C.A.G conceptualized, designed, and executed the synthesis and characterization of the dinuclear and trinuclear polymethine dyes. E.Y.L and E.B.M performed all imaging experiments. K.M.H performed nucleophilic susceptibility experiments. A.L and E.Y.L performed cell experiments. E.M.S primarily supervised the study, along with J.A.A. C.A.G, E.Y.L, E.B.M, and E.M.S contributed to writing. All authors have edited and approved the manuscript.

Acknowledgements

This material is based upon work partially supported by the National Science Foundation Graduate Research Fellowship Program under Grant Number. DGE-2034835 (Cesar A. Garcia). Any opinions, findings, and conclusions or recommendations expressed in this material are those of the authors and do not necessarily reflect the views of the National Science Foundation. We also acknowledge National Science Foundation (CHE-2204263 to Ellen M. Sletten), the National Institute of Biological Imaging and Bioengineering (1R01EB027172 to Ellen M. Sletten), the National Institute of Environmental Health Sciences (R01ES032806 to Jesus A. Araujo), the Tobacco Related Disease Program (T32DT4847 to Eric Y. Lin), the UCLA Jonsson Comprehensive Cancer Center (Emily B. Mobley), and the UCLA Graduate Division (Eric Y. Lin, Emily B. Mobley, and Allen Louie) for financial support. We also extend our gratitude to Dr. Yuh Guo Pan and Charles J. Pederson for fellowships to Cesar A. Garcia. The work was supported by shared instrumentation grants from the National Science Foundation (CHE-1048804) and NIH (S10OD028644). We thank Laurent A. Bentolila for allocation of imaging lab space within the Advanced Light Microscopy and Spectroscopy Laboratory in CNSI at UCLA. Finally, we would like to thank Helen H. Lin for her assistance with statistical analysis of ex vivo fluorescence data.

Conflicts of Interest

The authors declare no conflicts of interest.

Data Availability Statement

The data that support the findings of this study are openly available in BioImage Archive at https://www.ebi.ac.uk/biostudies/BioImages/studies/S-BIAD2360?query=S-BIAD2360, reference number 2360.

References

1. M. J. Schnermann and L. D. Lavis, "Rejuvenating Old Fluorophores With New Chemistry," *Current Opinion in Chemical Biology* 75 (2023): 102335, https://doi.org/10.1016/j.cbpa.2023.102335.

2. K. Ilina and M. Henary, "Cyanine Dyes Containing Quinoline Moieties: History, Synthesis, Optical Properties, and Applications," *Chemistry – A European Journal* 27 (2021): 4230–4248, https://doi.org/10.1002/chem.202003697.

3. A. A. Ishchenko, "Structure and Spectral-Luminescent Properties of Polymethine Dyes," *Russian Chemical Reviews* 60 (1991): 865–884, https://doi.org/10.1070/RC1991v060n08ABEH001116.

4. H. Mustroph, "Polymethine Dyes," *Physical Sciences Reviews* 5 (2020): 20190084.

5. J. L. Bricks, A. D. Kachkovskii, Y. L. Slominskii, A. O. Gerasov, and S. V. Popov, "Molecular Design of Near Infrared Polymethine Dyes: A Review," *Dye Pigment* 121 (2015): 238–255, https://doi.org/10.1016/j.dyepig.2015.05.016.

6. H. Li, Y. Kim, H. Jung, J. Y. Hyun, and I. Shin, "Near-Infrared (NIR) Fluorescence-Emitting Small Organic Molecules for Cancer Imaging and Therapy," *Chemical Society Reviews* 51 (2022): 8957–9008, https://doi.org/10.1039/D2CS00722C.

7. A. S. Tatikolov, "Polymethine Dyes as Spectral-Fluorescent Probes for Biomacromolecules," *Journal of Photochemistry and Photobiology C: Photochemistry Reviews* 13 (2012): 55–90, https://doi.org/10.1016/j.jphotochemrev.2011.11.001.

8. X. Ma, L. Shi, B. Zhang, L. Liu, Y. Fu, and X. Zhang, "Recent Advances in Bioprobes and Biolabels Based on Cyanine Dyes," *Analytical and*

Bioanalytical Chemistry 414 (2022): 4551–4573, https://doi.org/10.1007/s00216-022-03995-8.

9. E. Thimsen, B. Sadtler, and M. Y. Berezin, "Shortwave-Infrared (SWIR) Emitters for Biological Imaging: A Review of Challenges and Opportunities," *Nanophotonics* 6 (2017): 1043–1054, https://doi.org/10.1515/nanoph-2017-0039.

10. B. Li, M. Zhao, and F. Zhang, "Rational Design of Near-Infrared-II Organic Molecular Dyes for Bioimaging and Biosensing," *ACS Materials Letters* 2 (2020): 905–917, https://doi.org/10.1021/acsmaterialslett.0c00157.

11. H. Zhang, D. C. Salo, D. M. Kim, S. Komarov, Y. C. Tai, and M. Y. Berezin, "Penetration Depth of Photons in Biological Tissues From Hyperspectral Imaging in Shortwave Infrared in Transmission and Reflection Geometries," *Journal of Biomedical Optics* 21 (2016): 126006, https://doi.org/10.1117/1.JBO.21.12.126006.

12. S. M. Usama and K. Burgess, "Hows and Whys of Tumor-Seeking Dyes," *Accounts of Chemical Research* 54 (2021): 2121–2131, https://doi.org/10.1021/acs.accounts.0c00733.

13. Y. Ma, C. Qin, Y. Lei, X. Yang, and Z. Lei, "Tissue-Seeking Dyes for *In Vivo* Applications," *Smart Molecules* 2 (2024): e20240029, https://doi.org/10.1002/smo.20240029.

14. S. Hameed, H. Chen, M. Irfan, et al., "Fluorescence Guided Sentinel Lymph Node Mapping: From Current Molecular Probes to Future Multimodal Nanoprobes," *Bioconjugate Chemistry* 30 (2019): 13–28, https://doi.org/10.1021/acs.bioconjchem.8b00812.

15. Y. Tajima, K. Yamazaki, Y. Masuda, et al., "Sentinel Node Mapping Guided by Indocyanine Green Fluorescence Imaging in Gastric Cancer," *Annals of Surgery* 249 (2009): 58–62, https://doi.org/10.1097/SLA.0b013e3181927267.

16. Y. Park, M. H. Park, and H. Hyun, "Structure-Inherent Tumor-Targeted IR-783 for Near-Infrared Fluorescence-Guided Photothermal Therapy," *International Journal of Molecular Sciences* 25 (2024): 5309, https://doi.org/10.3390/ijms25105309.

17. C. Zhang, L. Long, and C. Shi, "Mitochondria-Targeting IR-780 Dye and Its Derivatives: Synthesis, Mechanisms of Action, and Theranostic Applications," *Advances in Therapy* 1 (2018): 1800069, https://doi.org/10.1002/adtp.201800069.

18. C. Shi, J. B. Wu, and D. Pan, "Review on near-infrared Heptamethine Cyanine Dyes as Theranostic Agents for Tumor Imaging, Targeting, and Photodynamic Therapy," *Journal of Biomedical Optics* 21 (2016): 050901, https://doi.org/10.1117/1.JBO.21.5.050901.

19. S. Luo, X. Tan, Q. Qi, et al., "A Multifunctional Heptamethine Near-Infrared Dye for Cancer Theranosis," *Biomaterials* 34 (2013): 2244–2251, https://doi.org/10.1016/j.biomaterials.2012.11.057.

20. S. Jia, E. Y. Lin, E. B. Mobley, et al., "Water-Soluble Chromenylium Dyes for Shortwave Infrared Imaging in Mice," *Chemistry* 9 (2023): 3648–3665, https://doi.org/10.1016/j.chempr.2023.08.021.

21. A. P. Demchenko, Z. N. Volovik, Y. L. Briks, and A. D. Kachkovsky, "Cyanine Dyes With Branched (Trinuclear) Polymethine Chains: Long-Wavelength Biomembrane Probes," *SPIE* 2388 (1995): 273–279.

22. F. M. Hamer, R. J. Rathbone, and B. S. Winton, "271. Some Trinuclear Cyanine Dyes. Part I. The Synthesis of Neocyanines," *Journal of the American Chemical Society* (1947): 1434, https://doi.org/10.1039/jr9470001434.

23. H. John, C. Briehn, J. Schmidt, S. Hünig, and J. Heinze, "Trinuclear Cyanines (TNCs) Revisited: A New Class of Electrochromics by Intramolecular π/σ Switching," *Angewandte Chemie International Edition* 46 (2007): 449–453, https://doi.org/10.1002/anie.200602596.

24. A. Mishra, R. K. Behera, P. K. Behera, B. K. Mishra, and G. B. Behera, "Cyanines During the 1990s: a Review," *Chemical Reviews* 100 (2000): 1973–2011, https://doi.org/10.1021/cr990402t.

25. C. Reichardt, U. Budnik, K. Harms, G. Schäfer, and J. Stein, "Chiral Polymethine Dyes, V. syntheses, Absolute Configuration, Spectroscopic, and Chiroptical Properties of Chiral Dinuclear Tri- and Pentamethinium as Well as Trinuclear [2.2.2]Heptamethinediium Cyanine Dyes With 3-Sec -Butyl-1,3-Dimethylindolyl End Groups," *Liebigs Annalen* 1995 (1995): 329–340, https://doi.org/10.1002/jlac.199519950241.

26. K. Kohno, S. Koya-Miyata, A. Harashima, et al., "Inflammatory M1-Like Macrophages Polarized by NK-4 Undergo Enhanced Phenotypic Switching to an Anti-Inflammatory M2-Like Phenotype Upon Co-Culture With Apoptotic Cells," *Journal of Inflammation* 18 (2021): 1–14, https://doi.org/10.1186/s12950-020-00267-z.

27. S. Liu, T. Matsuo, and T. Abe, "Revisiting Cryptocyanine Dye, NK-4, as an Old and New Drug: Review and Future Perspectives," *International Journal of Molecular Sciences* 24 (2023): 4411, https://doi.org/10.3390/ijms24054411.

28. H. Ohta, S. Arai, K. Akita, T. Ohta, and S. Fukuda, "Effects of NK-4 in a Transgenic Mouse Model of Alzheimer's Disease," *PLoS ONE* 7 (2012): e30007, https://doi.org/10.1371/journal.pone.0030007.

29. E. D. Cosco, J. R. Caram, O. T. Bruns, et al., "Flavylium Polymethine Fluorophores for Near- and Shortwave Infrared Imaging," *Angewandte Chemie International Edition* 56 (2017): 13126–13129, https://doi.org/10.1002/anie.201706974.

30. E. D. Cosco, B. A. Arús, A. L. Spearman, et al., "Bright Chromenylium Polymethine Dyes Enable Fast, Four-Color *In Vivo* Imaging With Shortwave Infrared Detection," *Journal of the American Chemical Society* 143 (2021): 6836–6846, https://doi.org/10.1021/jacs.0c11599.

31. E. D. Cosco, A. L. Spearman, S. Ramakrishnan, et al., "Shortwave Infrared Polymethine Fluorophores Matched to Excitation Lasers Enable Non-Invasive, Multicolour *In Vivo* Imaging in Real Time," *Nature Chemistry* 12 (2020): 1123–1130, https://doi.org/10.1038/s41557-020-00554-5.

32. C. A. Garcia, E. B. Mobley, E. Y. Lin, K. Bui, and E. M. Sletten, "Palladium-Catalyzed Functionalization of Shortwave Infrared Heptamethine Fluorophores Expands Their *In Vivo* Utility," *Journal of the American Chemical Society Au* 5 (2025): 2089–2101, https://doi.org/10.1021/jacsau.4c01279.

33. E. B. Mobley, E. Y. Lin, and E. M. Sletten, "Chromenylium Star Polymers: Merging Water Solubility and Stealth Properties With Shortwave Infrared Emissive Fluorophores," *ACS Central Science* 11 (2025): 208–218, https://doi.org/10.1021/acscentsci.4c01570.

34. A. L. Spearman, E. Y. Lin, E. B. Mobley, et al., "High-Resolution Multicolor Shortwave Infrared Dynamic *In Vivo* Imaging With Chromenylium Nonamethine Dyes," *Journal of the American Chemical Society* 147 (2025): 17384–17393, https://doi.org/10.1021/jacs.5c03673.

35. H. Lee, M. Y. Berezin, M. Henary, L. Strekowski, and S. Achilefu, "Fluorescence Lifetime Properties of Near-Infrared Cyanine Dyes in Relation to Their Structures," *Journal of Photochemistry and Photobiology A: Chemistry* 200 (2008): 438–444, https://doi.org/10.1016/j.jphotochem.2008.09.008.

36. N. P. Neme, T. L. C. Jansen, and R. W. A. Havenith, "Cyclopentene Ring Effects in Cyanine Dyes: A Handle to Fine-Tune Photophysical Properties," *Physical Chemistry Chemical Physics* 26 (2024): 6235, https://doi.org/10.1039/D3CP05219B.

37. K. Nakano, T. Konishi, and Y. Imamura, "Estimation of Maximum Absorption Wavelength of Polymethine Dyes in Visible and Near-Infrared Region Based on Time-Dependent Density Functional Theory," *Chemical Physics* 518 (2019): 15–24, https://doi.org/10.1016/j.chemphys.2018.11.002.

38. M. Imoto, Y. Matsui, M. Takeda, et al., "A Probable Hydrogen-Bonded Meisenheimer Complex: An Unusually High S_NAr Reactivity of Nitroaniline Derivatives With Hydroxide Ion in Aqueous Media," *Journal of Organic Chemistry* 76 (2011): 6356–6361, https://doi.org/10.1021/jo2007219.

39. M. Gazitúa, R. A. Tapia, R. Contreras, and P. R. Campodónico, "Effect of the Nature of the Nucleophile and Solvent on an S_NAr Reaction," *New Journal of Chemistry* 42 (2017): 260–264, https://doi.org/10.1039/C7NJ03212A.

40. Y. L. Bricks, A. A. Ishchenko, A. D. Kachkovski, and A. I. Tolmachev, "Nature of Electronic Transitions in Trinuclear Polymethine Dyes," *Dye Pigment* 8 (1987): 353–369, https://doi.org/10.1016/0143-7208(87)85025-8.

41. W. Grahn, "13C-NMR-spektren von Di- und Trinuclearen Polymethincyanin-farbstoffen," *Tetrahedron* 32 (1976): 1931–1939, https://doi.org/10.1016/0040-4020(76)85199-X.

42. R. Allmann, W. Grahn, J. Knecht, D. Kucharczyk, and C. Reichardt, "Synthesen mit Aliphatischen Dialdehyden, XXXIX. Über die Konformation Trinuclearer [2.2.2]Heptamethindiium-Cyaninfarbstoffe mit Indolin-Endgruppen," *Chemische Berichte* 118 (1985): 1295–1303, https://doi.org/10.1002/cber.19851180402.

43. H. Ihmels, S. Jiang, M. M. A. Mahmoud, H. Schönherr, D. Wesner, and I. Zamrik, "Fluorimetric Detection of G-Quadruplex DNA in Solution and Adsorbed on Surfaces With a Selective Trinuclear Cyanine Dye," *Langmuir* 34 (2018): 11866–11877, https://doi.org/10.1021/acs.langmuir.8b02382.

44. C. Elian, B. Mourot, C. Benbouziyane, et al., "Tris-Benzo[*cd*]Indole Cyanine Enables the NIR-Photosensitized Radical and Thiol-Ene Polymerizations at 940 Nm," *Angewandte Chemie International Edition* 62 (2023): e202305963, https://doi.org/10.1002/anie.202305963.

45. G. B. Behera, P. K. Behera, and B. K. Mishra, "Cyanine Dyes: Self Aggregation and Behaviour in Surfactants—A Review," *Journal of Surface Science and Technology* 23 (2007): 1–31.

46. M. U. Aziz, J. R. Eisenbrey, A. Deganello, et al., "Microvascular Flow Imaging: A State-of-the-Art Review of Clinical Use and Promise," *Radiology* 305 (2022): 250–264, https://doi.org/10.1148/radiol.213303.

47. P. S. Russell, R. Velivolu, V. E. Maldonado Zimbrón, et al., "Fluorescent Tracers for *In Vivo* Imaging of Lymphatic Targets," *Frontiers in Pharmacology* 13 (2022): 952581, https://doi.org/10.3389/fphar.2022.952581.

48. T. Desmettre, J. M. Devoisselle, and S. Mordon, "Fluorescence Properties and Metabolic Features of Indocyanine Green (ICG) as Related to Angiography," *Survey of Ophthalmology* 45 (2000): 15–27, https://doi.org/10.1016/S0039-6257(00)00123-5.

49. Z. Feng, X. Yu, M. Jiang, et al., "Excretable IR-820 for *In Vivo* NIR-II Fluorescence Cerebrovascular Imaging and Photothermal Therapy of Subcutaneous Tumor," *Theranostics* 9 (2019): 5706, https://doi.org/10.7150/thno.31332.

50. Y. Lu, E. Zhang, J. Yang, and Z. Cao, "Strategies to Improve Micelle Stability for Drug Delivery," *Nano Research* 11 (2018): 4985–4998, https://doi.org/10.1007/s12274-018-2152-3.

51. B. Zhao, X. Q. Wang, X. Y. Wang, et al., "Nanotoxicity Comparison of Four Amphiphilic Polymeric Micelles With Similar Hydrophilic or Hydrophobic Structure," *Particle and Fibre Toxicology* 10 (2013): 1–16, https://doi.org/10.1186/1743-8977-10-47.

Supporting Information

Additional supporting information can be found online in the Supporting Information section.

Chart S1, Tables S1 and S2, Schemes S1–S3, Figures S1–S14, Appendix Figures SA1–A44, Videos S1 and 2, experimental procedures for main text and supplementary figures, experimental data, and characterization of all new compounds are found within the supplementary info. All raw and processed in vivo imaging files can be found on BioImage Archive (https://www.ebi.ac.uk/biostudies/BioImages/studies/S-BIAD2360?query=S-BIAD2360), accession number: S-BIAD2360.

Supporting File 1: anie71499-sup-0001-SuppMat.pdf.